# Thermo-hydro-mechanical interactions in porous media: implications on thermo-active retaining walls

Eleonora Sailer[1], MEng MSc DIC, Postgraduate Researcher

David M.G. Taborda[1], MEng PhD DIC, Senior Lecturer

Lidija Zdravković[1], MEng MSc PhD DIC, Professor of Computational Geomechanics

David M. Potts[1], BSc PhD DSc, FREng FIC, FCGI, GCG Professor of Geotechnical Engineering

Wenjie Cui[2] *, BSc MSc PhD DIC, Associate Professor

[1]Department of Civil and Environmental Engineering, Imperial College London, UK

[2] School of Transportation Science and Engineering, Beihang University, Beijing 100191, China (formerly Imperial College London)

*Corresponding author: Wenjie Cui, School of Transportation Science and Engineering, Beihang University, Beijing 100191, China. Email address: wcui21@buaa.edu.cn

**Abstract**

Thermo-active structures exchange heat with the ground to provide thermal energy to buildings. Consequently, the ground is subjected to changes in temperature, inducing thermo-hydro-mechanical (THM) interactions within the soil. To provide insights into the origin and manifestations of the main mechanisms taking place in complex fully THM-coupled finite element (FE) analyses, simple, one-dimensional problems are firstly analysed in this paper and compared to analytical expressions developed for determining thermally-induced excess pore water pressures in undrained problems with different displacement restraints. Subsequently, various dimensionless parameters are established to evaluate the impact of varying ground properties on the observed THM interactions and their evolution with time. Finally, the findings from simple one-dimensional problems are verified in the context of THM modelling of thermo-active retaining walls, where the structural response of walls is shown to be highly transient and influenced by different phenomena prevailing over different periods involving thermal expansion of soils, volumetric deformations due to pore water generation and dissipation, and interactions with mechanical boundary conditions. The results also highlight the importance of performing fully coupled THM analyses and of a correct estimation of the hydraulic and thermal properties to guarantee a safe design of thermo-active structures.

**Keywords:** THM-coupled behaviour; Finite element modelling; Retaining walls; Porous media; Temperature effects; Soil-structure interaction

# 1 Introduction

Ground Source Energy Systems (GSES) provide sustainable heating and cooling to buildings (Brandl, 2006) and are increasingly being installed in densely built environments. These systems, which can be buried within geotechnical structures (such as foundation piles or walls), exchange heat with the ground at shallow depths (up to 300 m) and hence lead to a change in temperature of the surrounding soil mass. Thermo-active structures have been the subject of considerable research (e.g. Laloui et al., 2006; Bourne-Webb et al., 2009; Stewart and McCartney, 2013; Loveridge and Powrie, 2013; Ng et al., 2014; Makasis et al., 2018; Bourne-Webb et al., 2019; Sterpi et al., 2020) due to the uncertainty in their mechanical response when subjected to changes in temperature, and the need to guarantee their safety and serviceability, as well as that of any underground structure in their vicinity.

Typically, geotechnical structures are designed by means of numerical analyses, where the soil layers are explicitly modelled. Soils are multi-phase porous media, with saturated soils consisting of a mixture of solids and fluid, where the latter fills the pore space between the solid particles. Low permeability soils, such as clays, display a complex behaviour when subjected to temperature changes. Indeed, it was demonstrated by numerous laboratory studies undertaken on different types of clays, such as Pontida and Pasquasia clays (Baldi et al., 1988), Boom clay (Sultan et al., 2002), Kaolin (Cekerevac and Laloui, 2004) and soft Bangkok clay (Abuel-Naga et al., 2007a), that, when exposed to a temperature change, excess pore water pressures develop within the soil samples. As a consequence, their strength and stiffness will be affected. Thus, it is clear that when designing systems inducing temperature changes within the soil, numerous aspects of non-isothermal soil behaviour have to be considered. To model these in finite element (FE) simulations, fully coupled thermo-hydro-mechanical (THM) analyses are required, where the interaction between the three physical systems, i.e. the mechanical, hydraulic and thermal systems, is accounted for (Olivella et al., 1996; Lewis and Schrefler, 1998; Thomas and He, 1997; Gatmiri and Delage, 1997; Cui et al., 2018) . When compared to isothermal analyses (i.e. hydro-mechanical analyses), additional interactions occur in soils due to temperature changes, such as thermal expansion and temperature-induced pore fluid pressures. Moreover, mechanical constitutive models (e.g. Laloui and Francois, 2009; Abuel-Naga et al., 2007b) have also been developed to account for the

irreversible deformation (i.e. thermal plasticity) observed in laboratory tests when soils are subjected to temperature changes.

While several studies on soil-structure interaction by means of fully coupled THM analyses have been carried out for single thermo-active piles (e.g. Gawecka et al., 2017; Di Donna and Laloui, 2015; Liu et al., 2020) and groups of thermo-active piles (e.g. Dupray et al., 2014; Jeong et al., 2014), only limited literature exists on the THM behaviour of thermo-active retaining structures (Rui and Yin, 2018; Sailer et al., 2019a; Sailer et al., 2019b; Dai and Li, 2019; Barla et al., 2020). As a result, further research on thermo-active retaining walls is required, particularly as Sailer et al. (2019a) concluded that these structures display a highly transient behaviour and that their mechanical response is significantly affected by THM interactions taking place in the soil.

This study aims at characterising how complex coupled thermo-hydro-mechanical phenomena taking place in the soil affect the different aspects of soil-structure interaction under non-isothermal conditions occurring in a thermo-active retaining wall problem and identifying their impact on the structure's behaviour. For this purpose, simple one-dimensional problems are analysed first, to characterise the different mechanisms taking place in the soil. To assist in the interpretation of the results, analytical expressions for calculating excess pore water pressures resulting from changes in temperature in undrained conditions are developed. Furthermore, to evaluate the impact of ground properties on the observed THM interactions, various novel dimensionless parameters are established. Subsequently, the long-term behaviour of a thermo-active retaining wall is investigated, highlighting the influence on its response of the THM interactions identified in the simple one-dimensional problems. It should be noted that the conclusions are equally valid for other types of geothermal structures (e.g. piles or tunnel linings) and may be considered relevant when analysing existing or new underground structures in the proximity of a heat source.

All the analyses presented in this paper were performed using the Imperial College Finite Element Program (ICFEP, Potts and Zdravković (1999)), capable of modelling fully coupled THM behaviour (see Cui et al. (2018) for more details). As the focus of this work is the comprehensive characterisation of the fundamental THM-coupled phenomena occurring in the soil, thermo-plastic soil behaviour was

not taken into account. This option, similar to that adopted by existing studies (e.g. Di Donna et al., 2016; Salciarini et al., 2017; Rui and Yin, 2018), enables a simpler derivation of analytical expressions for estimating pore-water pressure generation under undrained conditions performed in this paper. The sign convention is such that positive values refer to tensile axial forces, bending moments as a result of tension on the excavated side of the wall and compressive pore water pressures.

## 2 Thermo-hydro-mechanical interactions in one-dimensional problems

Thermo-hydro-mechanical interactions are assessed by analysing two one-dimensional problems characterised by different mechanical and hydraulic boundary conditions, with the aim of representing the conditions within the retained (Problem A – one-dimensional expansion) and excavated (Problem B – fully restricted) sides of a thermo-active wall simulated in a 2D plane strain analysis (Figure 1).

It should be noted that the idealisation of the retained side assumes the soil mass is free to expand in the horizontal direction. This may not reproduce accurately the deformation mode of the soil mass in this region, where an important displacement in the vertical direction takes place. However, the adopted approximation of the problem offers the advantage of a simple one-dimensional model where the displacements occur in the same direction as heat transfer and water flow. Furthermore, it allows a useful comparison to be established with the analytical solutions for excess pore water pressure generation in one-dimensional elements proposed in the next section. Hence, the adopted simplification was deemed appropriate for the characterisation of the THM interactions occurring within the retained side.

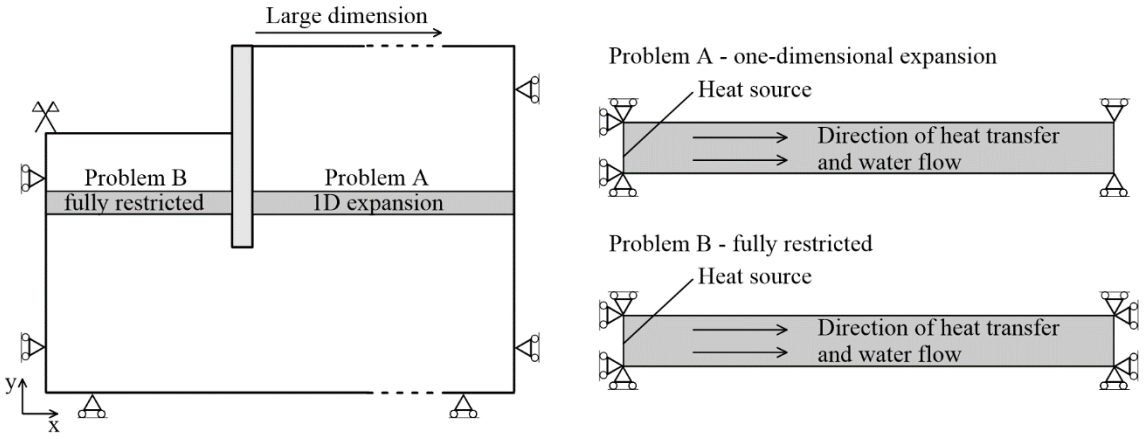



*Figure 1: Schematic representation of idealisation of one-dimensional problems in a retaining wall analysis*

## 2.1 Generation of excess pore water pressures

### 2.1.1 Hydraulic equation in coupled THM problems

The general hydraulic equation for a fully coupled THM analysis implemented in ICFEP, adopting a compression-positive sign convention, is expressed as (Cui et al., 2018):

$$\underbrace{-\nabla \cdot \{v_f\}}_{(i)} + \frac{n}{K_f}\frac{\partial u}{\partial t} \underbrace{- 3n(\alpha_w - \alpha_s)\frac{\partial T}{\partial t}}_{(ii)} + Q^f = \underbrace{\frac{\partial\left(\varepsilon_{v,tot} - \varepsilon_{v,th}\right)}{\partial t}}_{(iii)} \quad (1)$$

where $v_f$ is the vector of seepage velocity, $n$ is the porosity, $u$ is the pore water pressure, $K_f$ is the bulk modulus of the pore fluid, $\alpha_w$ and $\alpha_s$ are respectively the linear thermal expansion coefficients of the pore water and the soil skeleton, $T$ is temperature, $Q^f$ is any source or sink of pore fluid, $\varepsilon_{v,tot}$ and $\varepsilon_{v,th}$ are respectively the total and thermal volumetric strains (note that the difference between the two latter strains define the mechanical volumetric strains $\varepsilon_{v,mech} = \varepsilon_{v,tot} - \varepsilon_{v,th}$), and $t$ is time. If the presence of $Q^f$ is disregarded, there are three terms which define different mechanisms that contribute to the variation of pore water pressures in a coupled THM analysis (Cui et al., 2018):

- the term labelled as (i) represents pore water pressures changes due to water flow into and out of the soil element due to a hydraulic head gradient and is controlled by the permeability (or

hydraulic conductivity) of the soil (Darcy's law). The change in pore water pressures computed as a consequence of this phenomenon will be called "hydraulically-induced";

- the term labelled as (ii) calculates changes in pore water pressures as a result of the difference between the linear coefficients of thermal expansion of soil ($\alpha_s$) and water ($\alpha_w$). Since the latter is typically larger than the former, an increase in pore water pressures is observed during heating, with the opposite registered during cooling. The excess pore water pressures arising due to this mechanism will be designated as "thermally-induced";
- the term labelled as (iii) relates to the mechanism where changes in pore water pressures take place due to the variation of pore space arising from mechanical volumetric strains $\varepsilon_{v,mech}$ and these will be termed "mechanically-induced" (i.e. coupled-consolidation).

### *2.1.2 Analytical expressions for excess pore water pressures in undrained conditions*

Simple analytical expressions for the calculation of excess pore water pressures can be defined for soil subjected to undrained conditions. Under such conditions, it is assumed that no flow of water occurs, hence $v_f$ and $Q^f$ in Equation 1 are equal to zero. Furthermore, approximating $\partial\varepsilon_{v,tot}/\partial t$ as $\Delta\varepsilon_{v,tot}/\Delta t$, $\partial\varepsilon_{v,th}/\partial t$ as $\Delta\varepsilon_{v,th}/\Delta t$, $\partial u/\partial t$ as $\Delta u/\Delta t$ and $\partial T/\partial t$ as $\Delta T/\Delta t$, and noting that $\Delta\varepsilon_{v,mech} = \Delta p'/K_s$, Equation 1 can be re-written as:

$$\frac{\Delta u}{K_f} n - \underbrace{3n(\alpha_w - \alpha_s)\Delta T}_{(ii)} = \underbrace{\frac{\Delta p'}{K_s}}_{(iii)} \tag{2}$$

where $\Delta p'$, $\Delta u$ and $\Delta T$ are the changes in mean effective stress, pore water pressure and temperature, respectively, and $K_s$ is the bulk modulus of the soil skeleton. In Equation 2 – and in those in the following sections – the labels (ii) and (iii) refer to the mechanisms outlined in the previous paragraph.

*Single element representation of Problem A*

Problem A is represented by an element subjected to plane strain conditions being free to expand laterally in one direction only, as shown in Figure 2(a). Due to these mechanical restrictions, stress

changes will occur as a result of thermal soil expansion, leading to pore water pressure generation, which, for a linear-elastic material, can be quantified as follows (see Appendix A):

$$\Delta p' = \frac{2}{3}\left(\frac{\alpha_s \cdot \Delta T \cdot E - \Delta u \cdot \nu}{1-\nu}\right) - \frac{\Delta u}{3} \tag{3}$$

where $E$ is the Young's modulus and $\nu$ the Poisson's ratio.

Substituting the expression above into Equation 2 (noting that $3K_s = E/(1-2\nu)$) and rearranging, the excess pore water pressure calculated due to a change in temperature $\Delta T$ is equal to:

$$\Delta u = \underbrace{\frac{3n(\alpha_w - \alpha_s)\cdot \Delta T}{\frac{n}{K_f} + \frac{1}{3K_s}\left(\frac{1+\nu}{1-\nu}\right)}}_{(ii)} + \underbrace{\frac{2\alpha_s\left(\frac{1-2\nu}{1-\nu}\right)\cdot \Delta T}{\frac{n}{K_f} + \frac{1}{3K_s}\left(\frac{1+\nu}{1-\nu}\right)}}_{(iii)} \tag{4}$$

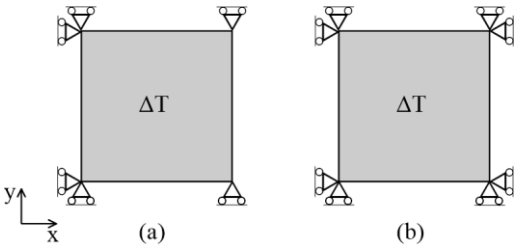
*Single element representation of Problem B*

Problem B is subjected to a further restriction in the lateral direction ($x$-direction, see Figure 2 (b)) compared to Problem A. Therefore, there will be an additional stress component, which leads to a change in mean effective stress, $\Delta p'$, equal to (see Appendix A):

$$\Delta p' = 3K_s \cdot \alpha_s \cdot \Delta T \tag{5}$$

Substituting this expression into Equation 2 and rearranging, the excess pore water pressure for a fully restricted soil element in undrained conditions is calculated as follows:

$$\Delta u = \underbrace{3(\alpha_w - \alpha_s)\cdot K_f \cdot \Delta T}_{(ii)} + \underbrace{3\alpha_s \cdot \frac{K_f}{n}\cdot \Delta T}_{(iii)} \tag{6}$$

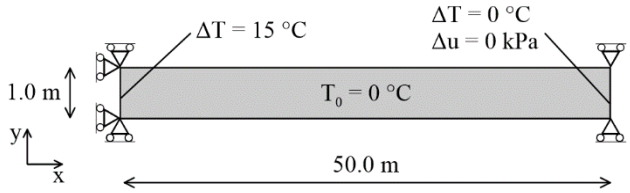



123

124 *Figure 2: Single element representation of (a) one-dimensional expansion and (b) fully restricted*

125 *2.2 Analysis of Problem A - One dimensional expansion*

126 As previously stated, Problem A aims at approximating the conditions within the retained side of a
127 thermo-active wall problem by considering a strip of soil analysed in plane-strain conditions which is
128 free to expand in the horizontal direction. The geometry is shown in Figure 3, where the finite element
129 mesh consists of 100 eight-noded quadrilateral elements, each 1.0 m in height and 0.5 m wide, with
130 displacement degrees of freedom at each node and pore water pressure and temperature degrees of
131 freedom at the corner nodes. The boundary conditions of the problem (see Figure 3) are as follows: a
132 constant temperature boundary condition of 15°C was applied at the nodes of the left-hand boundary to
133 model a source of heat, with no water flow allowed across this boundary; no changes in temperature
134 and pore water pressure were imposed at the right-hand boundary, simulating the conditions of a far
135 field boundary. To retain its characteristics as a one-dimensional problem, the nodes along the top and
136 bottom boundaries were free to displace laterally but not vertically and no heat flux or water flow was
137 allowed across these boundaries. An initial temperature of 0°C and hydrostatic pore water pressures
138 were assumed. The soil was considered linear-elastic and the material properties are outlined in Table
139 1. The total duration of the analysis was of 5 years and suitable time-steps were chosen according to
140 Cui et al. (2016) to avoid oscillations arising from thermal shock.




141

142 *Figure 3: Schematic of the analysed case of one-dimensional expansion*

| | | |
|---|---|---|
| Bulk modulus of soil skeleton [MPa] | $K_s$ | 83.3 |
| Poisson's ratio [-] | $\nu$ | 0.3 |
| Permeability [m/s] | $k$ | $1.0\times10^{-10}$ |
| Thermal conductivity [W/mK] | $\lambda$ | 2.0 |
| Volumetric heat capacity [kJ/m$^3$K] | $\rho C_p$ | 3000.0 |
| Coefficient of thermal expansion of soil [m/mK] | $\alpha_s$ | $1.0\times10^{-5}$ |
| Coefficient of thermal expansion of water [m/mK] | $\alpha_w$ | $6.9\times10^{-5}$ |
| Bulk modulus of fluid [GPa] | $K_f$ | 2.2 |
| Porosity [-] | $n$ | 0.5 |

*Table 1: Material properties of one-dimensional problems*

The changes in temperature and pore water pressures along the strip of soil at different time instants are displayed in Figure 4. For a single element subjected to a $\Delta T$ of 15 °C, the excess pore water pressures in undrained conditions calculated with Equation 4 are equal to 195.8 kPa. Conversely, the change in pore water pressures, and therefore in hydraulic head, generated at the heat source (i.e. $x$ = 0.0 m) in Problem A is equal to 80.4 kPa, i.e. less than half of the value computed with Equation 4. This indicates that the problem is not fully undrained and that water flow occurs due to the resulting pore water pressure gradient. Indeed, it can be noted that, as highlighted in Figure 4, further away from the heat source, excess pore water pressures develop even in regions where changes in temperature have not yet taken place, which are due to term (i) of Equation 1 (i.e. hydraulically-induced). Clearly, this suggests that, in the analysed problem, water flow is occurring at a faster rate than heat transfer, which, in the present case, is dominated by conduction. With time, as the heat front propagates and thus additional pore water pressures are generated due to changes in temperature, the hydraulically-induced excess pore water pressures increase as a larger volume of water flows through the soil mass towards the right-hand side boundary, which acts as a drain. At the heat source, the excess pore water pressures remain unaltered during the analysed time frame due to a combination of effects, the most important of which being the fact that the system has not yet reached thermal steady state, as seen in Figure 4 (a). This

means that in the vicinity of the heat source thermally-induced pore water pressures are continuously generated, compensating for any drainage taking place towards the drainage boundary, on the right-hand-side of the mesh. This balance between consolidation and heat conduction – and its role in the coupled THM phenomena taking place in this problem, is analysed in greater detail in Section 3.2.

In order to analyse the mechanically-induced excess pore water pressures, a further analysis was performed where $\alpha_w = \alpha_s = 1.0 \times 10^{-5}$. Hence, only term (iii) in Equation 1 and 4 contributes to the generation of pore water pressure as a consequence of temperature changes. In fully undrained conditions, the analytical solution in Equation 4 would suggest a rise in pore water pressures at the heat source of 22.4 kPa, which is approximately 90% less than in the previous case, indicating that the largest part of the generated excess pore water pressures is linked to the fact that $\alpha_w > \alpha_s$, i.e. are thermally-induced (term (ii) in Equation 1)**.** Similar to the previous case, the value obtained in the FE analysis is equal to 9.2 kPa, i.e. less than 50% of what is determined using the analytical solution. Moreover, the evolution with time of the distribution of pore water pressures within the soil strip are similar in shape to those calculated previously (i.e. $\alpha_w \neq \alpha_s$), though reduced in magnitude by approximately 90%. Thus, it can be concluded that the differential thermal expansion between the two soil phases (soil skeleton and pore fluid) affects the magnitude of the thermally and hydraulically induced excess pore water pressures, whereas their development with time is controlled by rate of dissipation and hence by the permeability of the material.

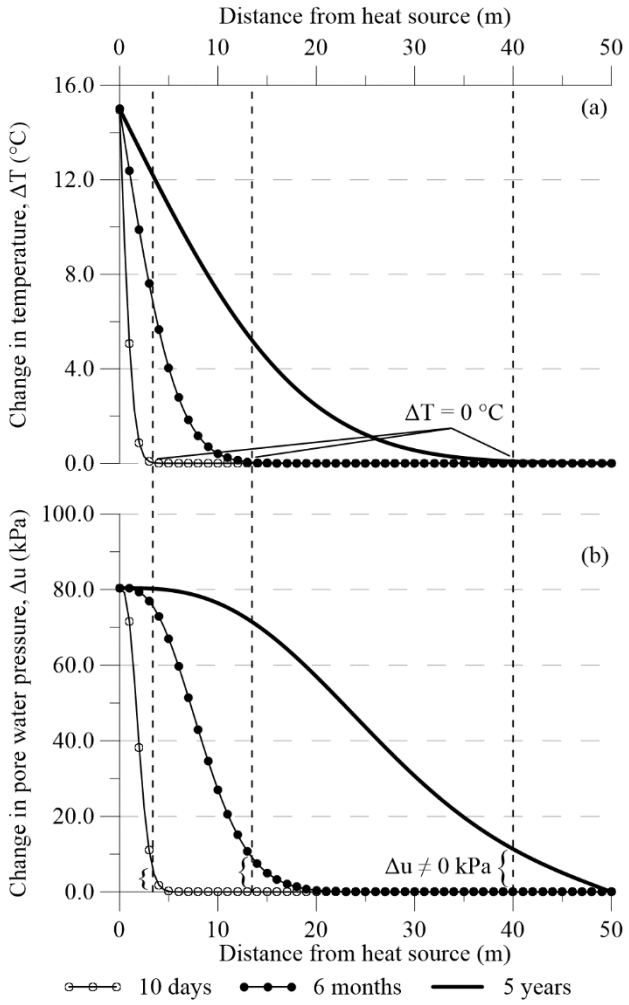



*Figure 4: One dimensional expansion – distributions with distance from heat source of (a) change in temperature ΔT and (b) change in pore water pressure Δu at three different time instants*

## *2.3 Analysis of Problem B - Fully restricted*

To simulate the soil conditions beneath the excavation, a similar case to the previous one (same material properties listed in Table 1) was analysed. The geometry of the problem is illustrated in Figure 5, where the same orientation and dimensions are adopted as in Problem A (i.e. 50 m long, heat source on the left-hand boundary) to allow for more direct comparisons between the two sets of analyses. The presence of the axis of symmetry on the boundary away from the heat source (right-hand boundary in the configuration shown in Figure 5) was modelled by introducing an additional mechanical restriction in the horizontal direction and by preventing water flow across the boundary. Moreover, while it is clear that symmetry considerations should have meant that no heat flux should be allowed across this

boundary, such option was discarded as it would reduce the scope for comparisons with Problem A. Therefore, a no change in temperature was imposed, meaning that, depending on the width of excavation, the adoption of this boundary condition may not reproduce accurately the temperature field beneath the excavation. However, it is considered appropriate for the purpose of identifying the fundamental mechanisms involved. All other boundary conditions are identical to those adopted in Problem A.

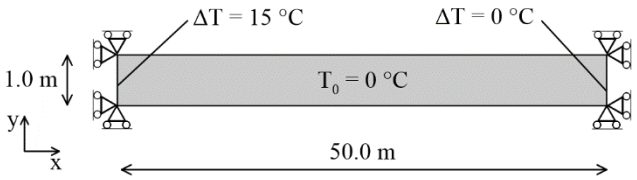



*Figure 5: Schematic of the fully restricted case*

The pore water pressure distributions calculated for this problem (Figure 6) are substantially different – both in terms of magnitude and variation with lateral extent – from those computed for Problem A. As expected, the pore water pressures are larger due to the larger mechanical volumetric strains resulting from the additional stress component in the horizontal direction (as shown by Equation 6). Furthermore, since water is not allowed to leave the system, pore water pressures accumulate over the entire horizontal distance, increasing with time as additional pore fluid pressures develop with further changes in temperature. In terms of comparison with the analytical solution (Equation 6), it should be noted that this was established assuming that the entire soil mass would change temperature simultaneously, which, as seen in Figure 6, does not correspond to the modelled thermal response in the FE analysis. It is therefore unsurprising that substituting $\Delta T = 15°C$ in Equation 6 returns significantly higher values of pore water pressure (i.e. 7821 kPa). A more adequate comparison consists of using in Equation 6 the average temperature at a given time instant obtained in the FE analysis (Figure 6 (a)). The predicted change in pore pressure is then in good agreement with the average pore water pressure computed in the FE analysis: for example, after 5 years, the average temperature change across the entire soil domain is equal to 3.47° (Figure 6 (a)), which, according to Equation 6, should result in excess pore water pressures of 1809 kPa. This value is in excellent agreement with the average excess pore water pressures

computed in the FE analysis, which are equal to 1804 kPa (Figure 6 (b)), demonstrating the value of this analytical approach in the interpretation of the complex coupled phenomena taking place in the soil mass.

Lastly, it is interesting to point out that, when assuming $\alpha_w = \alpha_s$, the calculated pore water pressures close to the heat source are approximately 25% of those shown in Figure 6, a slightly larger proportion than that determined in Problem A (10%).

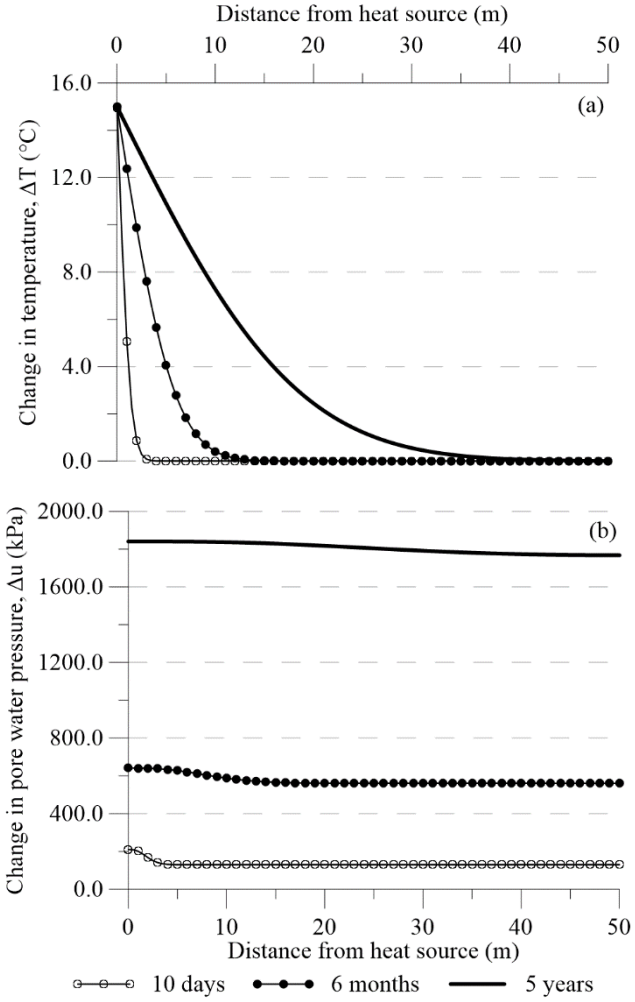



*Figure 6: Fully restricted – distributions with distance from heat source of (a) change in temperature $\Delta T$ and (b) change in pore water pressure $\Delta u$ at three different time instants*

# 3 Influence of soil properties on THM interactions

## *3.1 Dimensionless parameters*

### *3.1.1 Relative thermo-hydraulic diffusivity*

As demonstrated by the results of the simplified problems analysed in the previous section, the significance and nature of THM interactions are related to the rates of heat transfer and water flow, which are controlled, respectively, by the thermal and hydraulic diffusivity of the soil. The differential equation of one-dimensional heat transfer by conduction is expressed by Equation 7:

$$\frac{\partial T}{\partial t} = \alpha_T \frac{\partial^2 T}{\partial x^2} \tag{7}$$

where $\alpha_T$ is the thermal diffusivity [m$^2$/s], which is defined as the ratio of the thermal conductivity $\lambda$ [W/mK] and volumetric heat capacity $\rho C_p$ [J/m$^3$K].

Similarly, the differential equation of one-dimensional consolidation is defined as:

$$\frac{\partial u_e}{\partial t} = \alpha_H \frac{\partial^2 u_e}{\partial x^2} \tag{8}$$

where $\alpha_H$ is the hydraulic diffusivity [m$^2$/s], which is often also referred to as the coefficient of consolidation $c_v$, and $u_e$ is excess pore water pressure (kPa). The hydraulic diffusivity can be expressed as:

$$\alpha_H = \frac{k}{S_s} \tag{9}$$

with $k$ [m/s] being the permeability and $S_s$ [1/m] the specific storage, which is defined as (Jorgensen, 1980)

$$S_s = \rho_w g \left( \frac{n}{K_f} + \frac{1}{K_s} \right) \tag{10}$$

where $\rho_w$ is the density of water [kg/m$^3$], $g$ the specific gravity [m/s$^2$], $n$ the porosity [adim], and $K_f$ and $K_s$ are the bulk moduli [kN/m$^2$] of the pore fluid and the soil skeleton, respectively.

To measure the relative rates between the two phenomena, the dimensionless parameter $\alpha_{TH}$ is introduced:

$$\alpha_{TH} = \frac{\alpha_T}{\alpha_H} \tag{11}$$

Clearly, given its analytical definition, the variation of $\alpha_{TH}$ is mainly controlled by the value of the permeability, $k$, as all other material properties vary within a significantly more limited range.

### *3.1.2 Degree of heat transfer*

As previously outlined, the thermal diffusivity controls the rate of heat transfer. Thus, analyses with different values of $\alpha_T$ but equal thermal boundary conditions, will reach thermal equilibrium at different time instances. For the purpose of comparing such problems, the dimensionless parameter $R$ is introduced, establishing a parallel with the theory of one-dimensional consolidation. By using this parameter, the same temperature distributions are considered for analyses with different values of $\alpha_T$, even if that corresponds to different time instances. Furthermore, it allows the determination of how far the problem is from steady state. Indeed, similar to the average degree of consolidation (Craig, 2004), the average degree of heat transfer $R$ indicates the ratio, in terms of a percentage, between the amount of heat transferred up to a given time instant and the total heat transfer required to reach steady state, and is expressed as:

$$R = \frac{\int_0^L \Delta T_e \, dx}{\int_0^L \Delta T_f \, dx} \tag{12}$$

where $\Delta T_e$ is the distribution of temperature change at a given time, $\Delta T_f$ is the final distribution of temperature change (i.e. at steady state, when $t \to \infty$) and $L$ is the length of the one-dimensional solid.

A value of $R = 0$ means that heat transfer has not yet begun, whereas a value of $R = 1$ implies that thermal steady state has been reached.

The distributions of $\Delta T_e$ and $\Delta T_f$, hence also the evolution of $R$ with time, depend on the initial conditions and the boundary conditions of the analysed problem. Assuming a uniform initial temperature of 0°C, with the temperature boundary conditions specified in the previous section, i.e. fixed temperatures on both boundaries (one being the heat source and the other the constant far field temperature), the temperature distribution at steady state, $\Delta T_f$, is triangular. Conversely, if no heat flux would be allowed through the boundary opposite the heat source (e.g. modelling an axis of symmetry, which would apply to Problem B), this would lead to a final temperature distribution which is constant and equal to the induced temperature at the heat source. Curves of the degree of heat transfer $R$ against the dimensionless time $F_o$ (i.e. Fourier number, expressed as $\alpha_T t/L^2$, where $t$ is time) for these two conditions are depicted in Figure 7, where the similarity to the consolidation curves can be clearly identified. Analytical solutions for the calculation of $\Delta T_e$ with the outlined boundary conditions are presented in Appendix B.

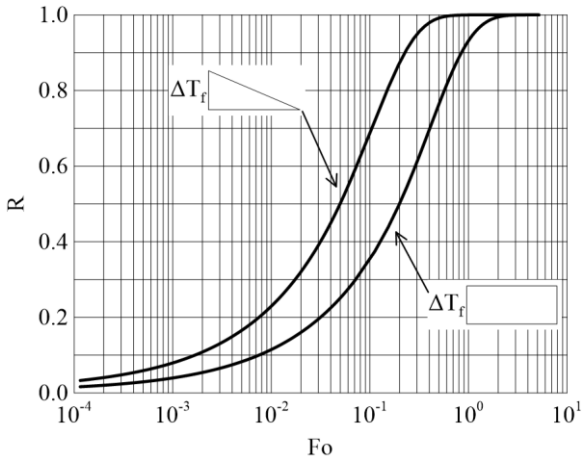



*Figure 7: Relationship between degree of heat transfer R and Fourier number*

### *3.1.3 Degree of pore water pressure generation*

*Thermally and mechanically induced excess pore water pressures*

At very small distances from the heat source, the soil elements are subjected to an almost-uniform temperature field and therefore the conditions of the single element represented in Figure 2 (a) are best reproduced. Thus, a comparison with the excess pore water pressures calculated through the analytical solutions in Section 2 can be performed. For this purpose, the following dimensionless parameter is introduced:

$$u^* = \frac{\Delta u_{FE}}{\Delta u_{AN}} \tag{13}$$

representing the ratio between the computed excess pore water pressure at the heat source in the FE analysis ($\Delta u_{FE}$) and the one obtained using the analytical solution ($\Delta u_{AN}$) expressed in Equation 4 (note that Equation 6 requires full mechanical restriction of the soil, which generally does not correspond to the conditions near the heat source). Hence, the parameter $u^*$ measures how undrained the problem is, with $u^*$ = 1 indicating a fully undrained case (i.e. the FE analysis yields the same result as the perfectly undrained problem assumed in the analytical solution) and $u^*$= 0 meaning that any generated excess pore water pressures have dissipated.

*Hydraulically-induced excess pore water pressures*

In order to quantify the amount of excess pore water pressures generated ahead of changes in temperature due to water flow, a further dimensionless parameter, $\omega$, is defined, with the parameters needed for its calculation being schematically represented in Figure 8. The parameter $\omega$ evaluates the percentage of excess pore water pressures computed at a given value of $R$ and $x$-coordinate where changes in temperature have not yet occurred ($\Delta u_{R,x(\Delta T=0°C)}$) with respect to the maximum excess pore water pressure generated during the analysis ($\Delta u_{max}$, typically at the start of the analysis, i.e. $R = 0$, and at the heat source ($x$ = 0.0)):

$$\omega = \frac{\Delta u_{R,x(\Delta T=0°C)}}{\Delta u_{max}} \tag{14}$$

This parameter is needed to consistently compare the amount of hydraulically-induced excess pore water pressures between analyses characterised by different values of $\alpha_{TH}$.

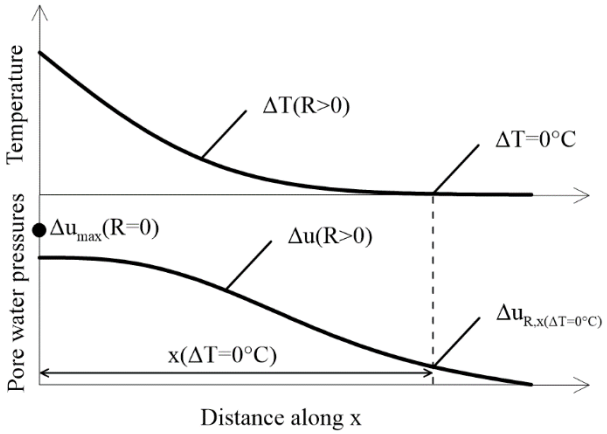



*Figure 8: Schematic representation of calculation of ω*

## *3.2 Parametric study on Problem A*

A parametric study on the influence of $\alpha_{TH}$ on the different mechanisms involving pore pressure generation and dissipation, i.e. those due to changes in temperature and those due to water flow, was carried out on Problem A. Different values of $\alpha_{TH}$ were analysed by varying the permeability, as shown in Table 2, with the values for all other parameters remaining as listed in Table 1. Moreover, additional analyses were carried out where other parameters were varied (e.g. thermal conductivity) in order to obtain the same value of $\alpha_{TH}$. The results showed that, despite the different combination of parameters, the same response was obtained, confirming that $\alpha_{TH}$ controls the magnitude of the THM interactions.

| $k$ [m/s] | $\alpha_{TH}$ |
|---|---|
| $1.0\times10^{-14}$ | $8.0\times10^{3}$ |
| $1.0\times10^{-12}$ | $8.0\times10^{1}$ |
| $1.0\times10^{-10}$ | $8.0\times10^{-1}$ |
| $1.0\times10^{-9}$ | $8.0\times10^{-2}$ |
| $1.0\times10^{-8}$ | $8.0\times10^{-3}$ |
| $1.0\times10^{-7}$ | $8.0\times10^{-4}$ |

| | |
|---|---|
| $1.0\times10^{-6}$ | $8.0\times10^{-5}$ |
| $1.0\times10^{-5}$ | $8.0\times10^{-6}$ |

*Table 2: Performed analyses for parametric study on the influence of $\alpha_{TH}$*

### *3.2.1 Influence of $\alpha_{TH}$ on excess pore water pressures at the heat source*

Figure 9 shows the variation with $\alpha_{TH}$ of $u^*$ calculated at the first increment of the analysis (i.e. $R \cong 0$), where $\Delta u_{AN}$ was obtained using Equation 4. The results show that, for high values of $\alpha_{TH}$, the ratio $u^*$ is unity, meaning that the FE analysis yields pore water pressures identical to those predicted by the analytical solution. This suggests, as expected, that soils characterised by large values of $\alpha_{TH}$ display an undrained behaviour when subjected to temperature changes. As the value of $\alpha_{TH}$ reduces, $u^*$ decreases, reaching a value of 0 at very low $\alpha_{TH}$. Indeed, for such magnitudes of $\alpha_{TH}$, no or very little excess pore water pressures are generated due to the rate of pore water pressure dissipation being significantly higher than that of heat transfer.

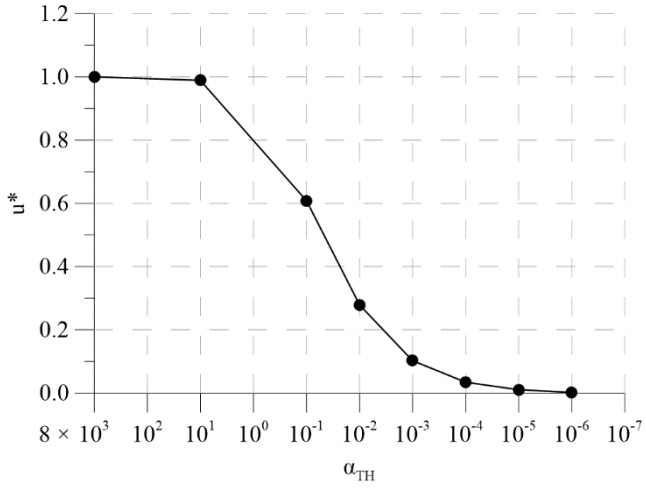



*Figure 9: Variation of $u^*$ at the heat source at beginning of the analysis with $\alpha_{TH}$*

Figure 10 shows the evolution of $u^*$ at the heat source with $R$ for selected values of $\alpha_{TH}$. For very high values of $\alpha_{TH}$, the curve remains approximately constant at a value of $u^*$= 1, starting to drop only as thermal steady state approaches (i.e. $R$ = 1). This indicates that, with high $\alpha_{TH}$, dissipation of pore water pressures occurs only when no further changes in temperature take place. As the value of $\alpha_{TH}$ decreases, the value of $R$ at which $u^*$ starts reducing also decreases, meaning that excess pore water pressure dissipation starts earlier and while temperature changes are still occurring. Indeed, a low value of $\alpha_{TH}$

indicates that water flow is faster when compared to heat transfer, with the time needed to reach hydraulic equilibrium being less than that required for achieving thermal steady state.

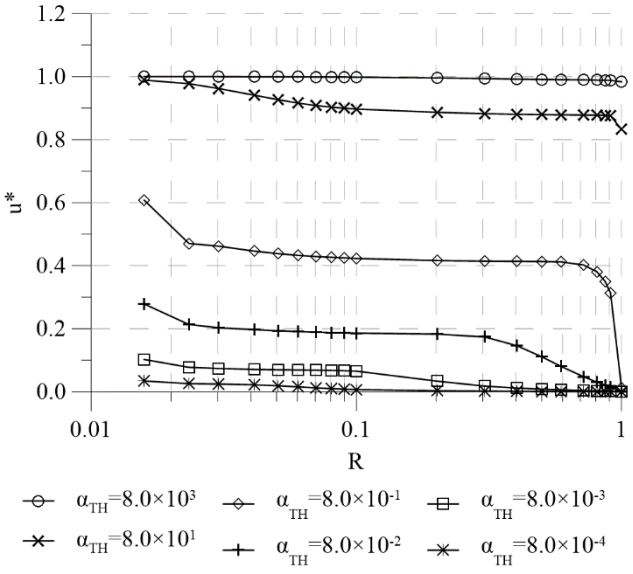



*Figure 10: Variation of u* at heat source with R for different $\alpha_{TH}$*

### *3.2.2 Influence of $\alpha_{TH}$ on hydraulically-induced excess pore water pressures*

To investigate the influence of $\alpha_{TH}$ on the amount of pore water pressures generated prior to changes in temperature, two time instants corresponding to two values of $R$ were considered, namely $R$ = 0.1 and $R$ = 0.5. For these stages of the analysis, the variations of $\omega$ with $\alpha_{TH}$ are shown in Figure 11, demonstrating that hydraulically-induced excess pore water pressures are also largely influenced by the value of $\alpha_{TH}$. It should be noted that the position of the heat front was established at the $x$-coordinate of the first node where the change in temperature, $\Delta T$, is less than 0.002°C.

At time instant $R$ = 0.1, for high values of $\alpha_{TH}$, $\omega$ is equal to 0, since, as previously observed, such values of $\alpha_{TH}$ lead to an undrained soil response, hence low water flow. Similarly, for very low values of $\alpha_{TH}$, $\omega$ is very small. In this case, excess pore water pressures are immediately dissipated given the higher rate of water flow when compared to heat transfer. It should be noted that, although the lowest value of $\alpha_{TH}$ still displays a $\omega$ of about 5%, this corresponds to negligible pore water pressures in absolute terms as the ones generated at the heat source ($\Delta u_{max}$) are very small (see Figure 9). For

intermediate values of $\alpha_{TH}$, $\omega$ reaches values of up to of 70%, indicating that the balance between the thermal and hydraulic systems is such that water flow occurs at a sufficiently fast pace that leads to excess pore water pressures in regions where no changes in temperature have yet taken place. Hence, it can be expected that for these combinations of parameters, excess pore water pressures may develop up to considerable distances away from a heat source.

For $R$ = 0.5, $\omega$ is very low for all the analyses, because, as time progresses and heat propagates, larger amounts of pore water pressures dissipate and leave the system through the right-hand boundary. It is interesting to note that the peak of the curve of $\omega$ shifts to a different value of $\alpha_{TH}$ with increasing $R$, thus a direct correlation between $\omega$ and $\alpha_{TH}$ cannot be established as this mechanism is time-dependent. In fact, $\omega$ for different values of $\alpha_{TH}$ varies differently with $R$: for a low value of $\alpha_{TH}$, $\omega$ varies more rapidly with $R$ in respect to soils with a high value of $\alpha_{TH}$ since, with those conditions, the pore water pressures dissipate at a faster rate, confirming the conclusions drawn from Figure 10.

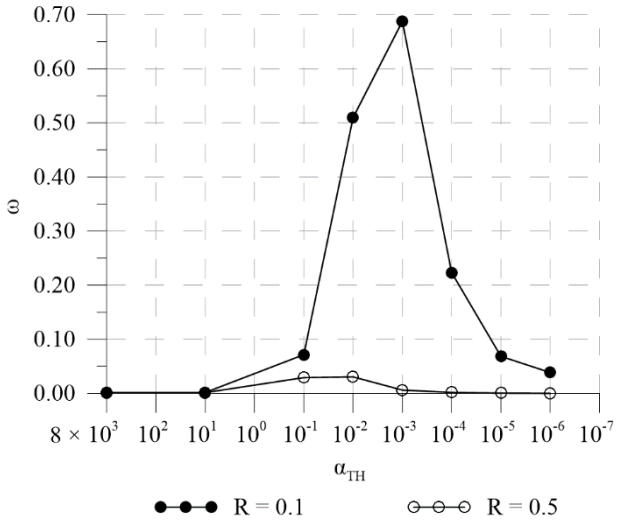



*Figure 11: Variation of ω with $\alpha_{TH}$ for R = 0.1 and R = 0.5*

## 4 Observed THM interactions in a thermo-active retaining wall problem

### *4.1 Problem description*

To illustrate the impact of the THM interactions on a thermo-active retaining wall, the problem studied by Sailer et al. (2019a) is re-analysed. This consists of an 18 m-deep and 800 mm-thick diaphragm wall

supporting an 11 m-deep excavation reported originally by Wood and Perrin (1984). The permanent horizontal structures include a concrete base slab (1.5 m thick) and the three additional slabs (350 mm thick). The geotechnical conditions – stratigraphy, pore water pressure regime and at-rest coefficient of earth pressure profile – are typical of those found in London and are described in detail in Sailer et al. (2019a), together with the adopted construction sequence. While this wall was not used as a heat exchanger, its response to excavation and construction was well characterised by the comprehensive monitoring system deployed at the site. This enabled Sailer et al. (2019a) to validate their numerical model for this retaining wall by showing a good agreement between the monitoring data and the FE predictions.

For brevity, only the essential characteristics of the thermal stage of the analysis are described here, with additional details being provided in Appendix C. Plane strain, fully coupled Thermo-Hydro-Mechanical (THM) analyses using ICFEP were carried out in this study. The FE mesh, shown in Figure 12, models half width of the excavation (30 m) and consists of eight-noded quadrilateral solid elements. Each node includes displacements and temperature degrees of freedom, whereas the elements representing consolidating materials (LC – London Clay and LGC – Lambeth Group Clay) have also pore pressure degrees of freedom associated to the corner nodes. The domain was restrained in the vertical direction along the bottom boundary and in the horizontal direction along the lateral and bottom boundaries. The Made Ground (MG), the Terrace Gravels (TGD) and Thanet Sand (TS) were simulated to be free-draining materials. Along the right-hand lateral boundary, hydraulic boundary conditions were such that no change in pore water pressure takes place. Furthermore, in order to simulate the presence of a drainage system, as reported by Wood and Perrin (1984), a pore water pressure of 0 kPa was prescribed along the interface between the underside of the base slab and the soil.

It is specified that prior to the application of the thermal load, the pore water pressures due to excavation and construction of the basement were fully dissipated in order to eliminate their effects on the subsequent THM analysis. The initial temperature was assumed to be 13°C and the heat exchange was simulated by applying a prescribed temperature change of 15°C over 10 days (i.e. 1.5°C/day) to all elements of the diaphragm wall, with the final temperature of 28°C being kept constant for 10 years.

The ground surface and the right-hand far field boundary were kept at constant temperature throughout the analysis, whereas no heat flux was allowed across all other boundaries of the domain and at the interface between the soil and the building.

All mechanical, hydraulic and thermal soil properties were adopted from Gawecka et al. (2017) and can be found in Appendix C.

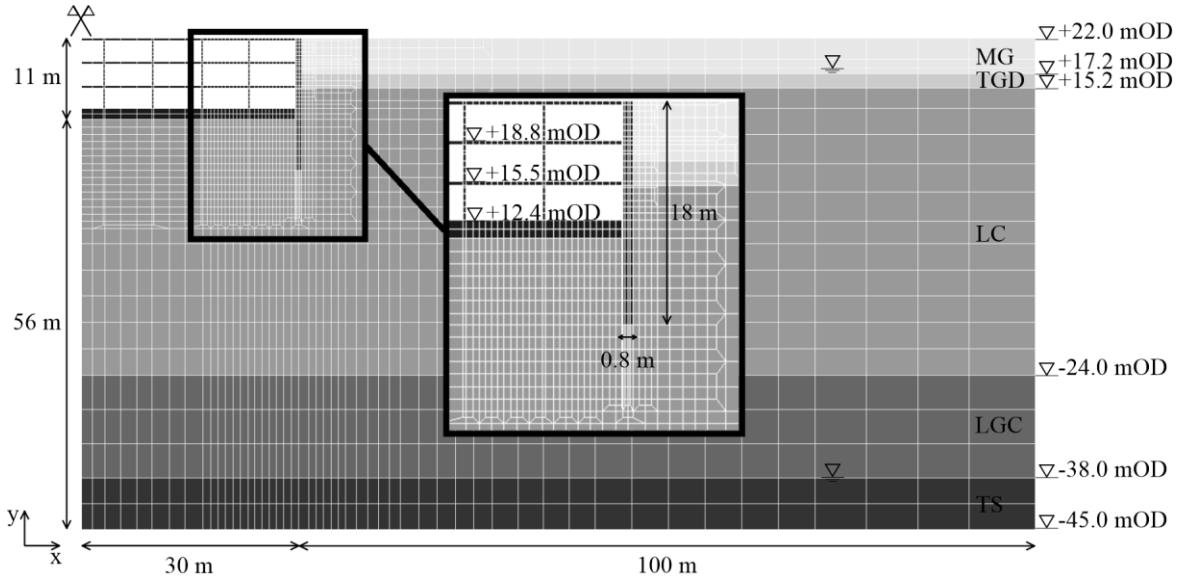



*Figure 12: FE Mesh for the analysed thermo-active retaining wall problem.*

## *4.2 Effects of THM interactions*

### *4.2.1 Pore water pressures*

The distributions of both changes in temperatures ($\Delta T$) and pore water pressures ($\Delta u$) along a horizontal line at mid-depth of the embedded part of the wall were computed for different time instants. These are shown for both the excavated and retained sides of the wall in Figure 13 (a) and (b), respectively. The three mechanisms of excess pore water pressure generation identified in Section 2 can be clearly observed in this complex boundary value problem and are marked in Figure 13 as: (i) due to water flow, (ii) induced by a temperature change, and (iii) as a consequence of a mechanical restriction (the latter being more evident in the excavated side due to the closer proximity to the boundary). Naturally, closer to the heat source pore water pressures are highest and driven mostly by temperature changes, as these are highest in this area of the problem. Moreover, the presence of additional drainage boundaries means

409 that pore-pressures around the heat source dissipate faster in the wall problem than in the simplified
410 one-dimensional problems considered in Section 2. At larger distances from the structure, $\Delta u$ develop
411 in areas where temperature changes have not yet taken place (i.e. $\Delta T$ = 0°C, marked in the figure as
412 "i"), as was observed when analysing Problem A. It is also particularly interesting to note the similarity
413 between the distributions of pore water pressures in the long term (10 years) beneath the excavated area
414 and those computed in Problem B (labelled as "iii" in Figure 13 (b)): the building up of a uniform profile
415 of excess pore water pressures is due to the mechanical restriction imposed at the axis of symmetry.
416 However, in the case of the retaining wall, when compared to the one-dimensional problem, the pore
417 water pressures tend to accumulate later in time and to be of lower magnitude due to the availability of
418 other drainage paths and the less effective mechanical restriction provided by the deforming soil mass.

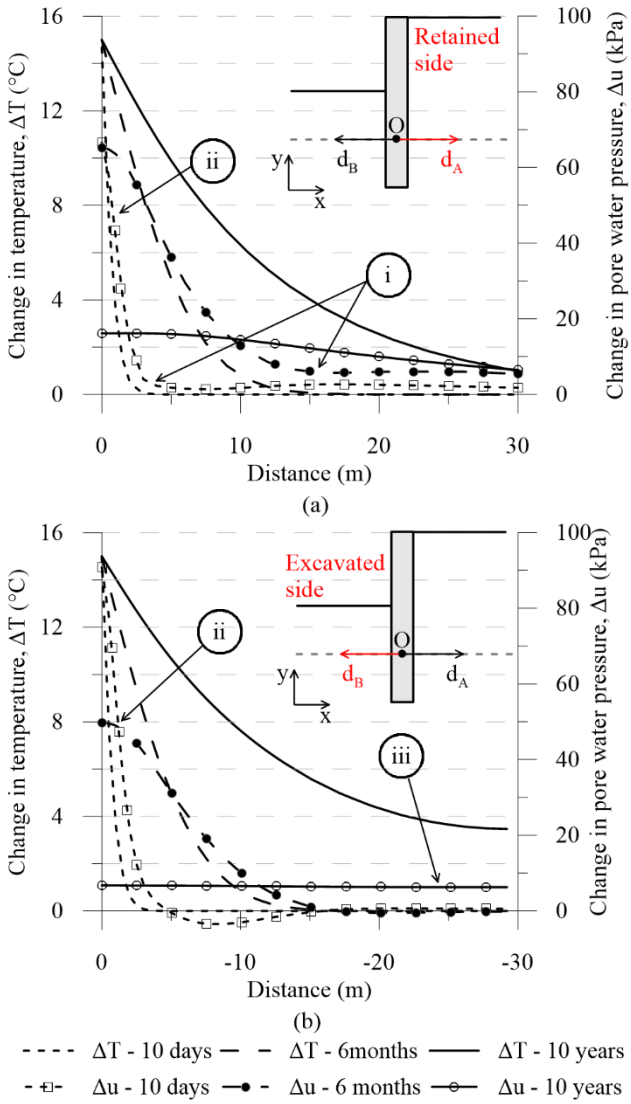



*Figure 13: Retaining wall problem - distribution of change in temperature ΔT and change in pore water pressure Δu at for different time instants on (a) the retained side and (b) the excavated side*

### *4.2.2 Structural forces*

The behaviour in terms of heat transfer and pore water pressure dissipation observed in the previous section are now analysed in terms of their impact on the structural forces in the wall, shown in Figure 14 from the start of the thermal stage (i.e. disregarding the forces due to excavation and construction). Specifically, Figure 14 (a) depicts the evolution of axial forces with time recorded at the point within the embedded part of the structure where the largest changes in axial forces take place (i.e. at a depth of 14.0m below ground level (bgl)). In Figure 14 (b) the development with time of the bending moment close to the base slab is displayed, as in this section the largest positive bending moment is calculated.

430 It can be noted that the evolution with time of forces is highly non-linear, as it is controlled by different
431 phenomena which prevail at different times. For reference, the maximum axial forces and bending
432 moments evaluated at these depths during excavation and construction are equal to 400 kN and 960
433 kNm, respectively.

434 Initially, when the wall is heated and consequently expands, the axial forces are compressive and
435 increase as further changes in temperature are applied (zone marked as "SR" – **S**oil **R**estriction – in
436 Figure 14 (a)). The compression is induced by the restriction the soil applies against the thermal
437 expansion of the wall through shearing at the soil-structure interface. It should be noted that at the same
438 time, the soil around the wall warms up and compressive excess pore water pressures are generated due
439 to the positive change in temperature (see Equation 2), which lead to tensile volumetric changes of the
440 soil, hence partially reducing the restriction. With time, as more heat is transferred to the soil, it
441 thermally expands, further reducing its restriction to the expansion of the wall. Indeed, in this time
442 frame (zone "TE" – **T**hermal **E**xpansion), the structure is subjected to tensile actions, which reduce the
443 initially generated compressive axial force and lead to the development of tensile forces within the
444 structure. Subsequently, the soil exerts compressive forces on the structure, reducing the tensile axial
445 force and producing a final value which is compressive and larger than the one generated during phase
446 "SR". This compression, highlighted in Figure 14 (a) as zone "DC" (**D**issipation and subsequent
447 **C**onsolidation), is caused by the dissipation of the compressive excess pore water pressures close to the
448 structure, which induces soil settlement and thus compression of the wall.

449 Similarly, the evolution of the bending moment with time can be divided into three different periods,
450 within which different mechanisms lead to changes in the bending moment (Figure 14 (b)). As
451 previously seen, the propagation of heat within the soil mass leads to soil expansion, which will occur
452 both in the vertical and horizontal direction. Since the temperatures are higher within the excavated side
453 due to insulated boundaries close to the heat source (i.e. the building and axis of symmetry), the soil
454 mass expands more in this area. As a consequence, the bottom of the wall moves towards the retained
455 soil. Therefore, in the time interval where soil thermal expansion dominates the problem (zone "TE" in
456 Figure 14 (b)), the bending moment increases. As the compressive excess pore water pressures dissipate

and the soil consequently contracts, the wall moves back towards its initial position and the bending moment decreases, which is marked as zone “DC”. There is a subsequent increase in bending moment which is due to further horizontal soil movements towards the retained soil. This movement, taking place in zone “BC” (effect of mechanical **B**oundary **C**ondition), is caused by the interaction of the thermal expansion of the soil with the lateral boundary, i.e. the axis of symmetry, where the imposed boundary conditions restrict horizontal movements, hence impeding further expansion in that direction. As seen previously for the pore water pressure mechanism “iii”, the effects of this mechanical restriction are experienced only once the heat front has reached the boundary. Hence, it can be concluded that, for a thermo-active retaining wall, the magnitude of bending moments, as well as pore water pressures within the excavated side, will be highly influenced by the width of the excavation.

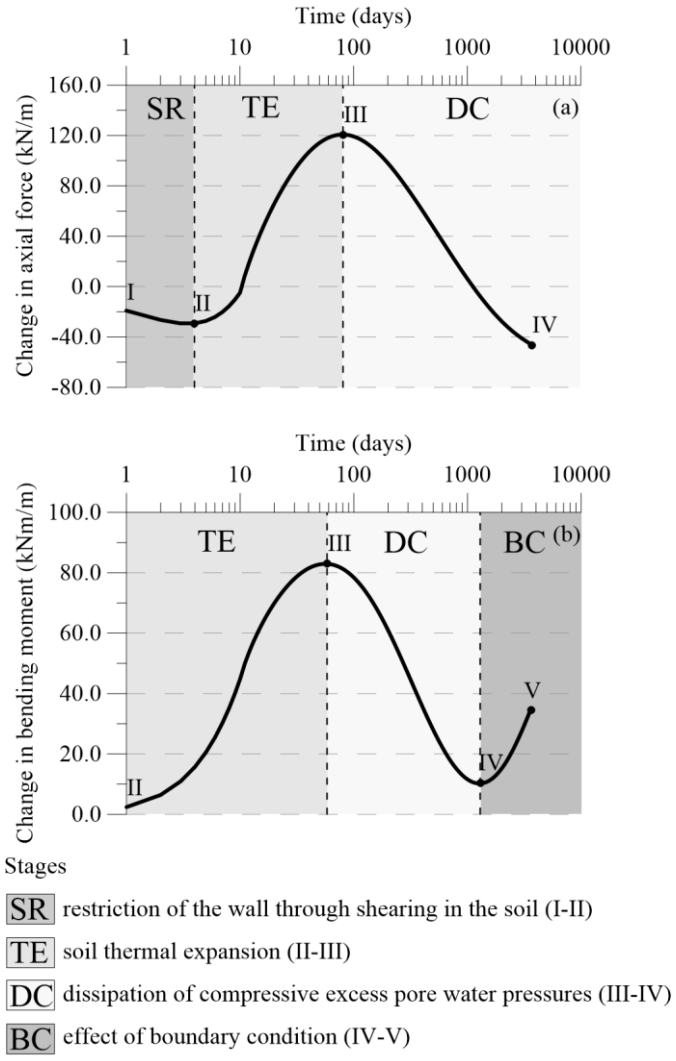



*Figure 14: Development with time of structural forces due to thermal loading: (a) axial force at depth of 14. 0 m bgl and (b) bending moment at depth of 10.5 m bgl*

### *4.3 Effect of $\alpha_{TH}$*

In section 3.2 it was shown that the parameter $\alpha_{TH}$ controls the development of the excess pore water pressures and hence the THM interactions in a simplified one-dimensional problem. Therefore, this section investigates the effect of varying this parameter on the response of the thermo-active retaining wall problem described above. Since the wall is embedded within different materials with different properties and the permeability of the consolidating materials was modelled as being stress-dependent (see Appendix C), a unique value of $\alpha_{TH}$ for the entire model cannot be established. Furthermore, the hydraulic diffusivity (Equation 9) depends on a further non-constant parameter, i.e. the bulk modulus of the soil $K_s$, which varies with both the stress level and the volumetric strain (Appendix C includes a

summary of the constitutive relations used). Therefore, as an approximation, the chosen values of permeability and mean effective stress were those at mid-depth of the embedded section of the wall (i.e. at 14.5 m depth, within London Clay) at the start of the thermal analysis, 1 m away from the wall on the retained side. Furthermore, the current value of the elastic bulk modulus, $K_s$, was approximated by its maximum value, $K_{max}$, given by the small strain stiffness model employed in the analysis (IC-G3S model, Taborda et al. (2016)):

$$K_{max} = K_0 \left( \frac{p'}{p'_{ref}} \right)^{m_k} \tag{15}$$

where $K_0$ and $m_k$ are model parameters listed in Appendix C, $p'$ is the mean effective stress evaluated at mid-depth of the embedded wall on the retained side (255.0 kPa) and $p'_{ref}$ is the reference mean effective stress (100.0 kPa). Similarly, the thermal parameters of London Clay were used to calculate $\alpha_T$.

Based on the methodology outlined above, values of $\alpha_H$ and $\alpha_T$ of $3.8 \times 10^{-7}$ m$^2$/s and $9.8 \times 10^{-7}$ m$^2$/s, respectively, were determined for the analysis presented in the previous section (denoted as "Base case" in Table 3). This leads to a ratio of $\alpha_{TH}$ of $2.6 \times 10^{0}$. To illustrate the impact of this parameter on the behaviour of the thermo-active retaining wall, two additional analyses were performed: one with a value of $\alpha_{TH}$ increased by two orders of magnitude (i.e. "high" in Table 3, $\alpha_{TH} = 2.6 \times 10^{2}$) and one where it is reduced by two orders of magnitude (i.e. "low" in Table 3, $\alpha_{TH} = 2.6 \times 10^{-2}$). As shown in Table 3, this was achieved by adjusting the parameters for the adopted permeability model.

| Analysis | $k_0$ [m/s] | $k_{emb}$ [m/s] | $\alpha_H$ [m$^2$/s] | $\alpha_T$ [m$^2$/s] | $\alpha_{TH}$ [-] |
|---|---|---|---|---|---|
| High | $1.0\times10^{-12}$ | $5.5\times10^{-13}$ | $3.8\times10^{-9}$ | $9.8\times10^{-7}$ | $2.6\times10^{2}$ |
| Base case | $1.0\times10^{-10}$ | $5.5\times10^{-11}$ | $3.8\times10^{-7}$ | | $2.6\times10^{0}$ |
| Low | $1.0\times10^{-8}$ | $5.5\times10^{-9}$ | $3.8\times10^{-5}$ | | $2.6\times10^{-2}$ |

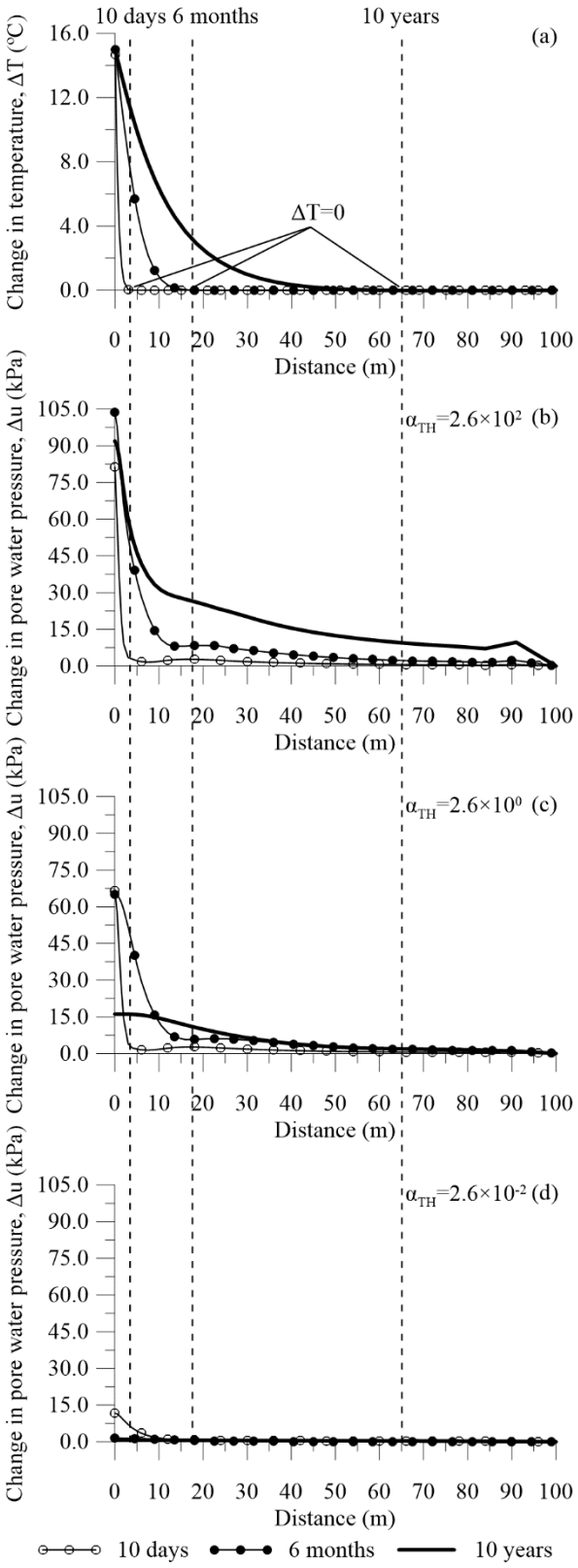
*Table 3: Parameters of parametric study for THM interactions in thermo-active retaining wall problem*

498 *4.3.1 Influence on pore water pressure generation*

499 Figure 15 depicts the temperature and pore water pressure distributions within the retained side at mid-
500 depth of the retaining wall for the three analyses at three different time instants. It can be clearly noted
501 that the magnitudes and evolution of pore water pressure generation are influenced by the value of $\alpha_{TH}$,
502 to an extent similar to that observed in the simplified one-dimensional problem (Problem A). In general,
503 the results show that higher thermally-induced pore water pressures are predicted for higher values of
504 $\alpha_{TH}$.

505 Regarding the pore water pressures generated in the vicinity of the heat source, these increase with
506 increasing $\alpha_{TH}$, as seen for Problem A, since larger values of $\alpha_{TH}$ correspond to problems where the
507 response is closer to being characterised as undrained. Moreover, in such cases, the dissipation with
508 time of these pore water pressures is significantly slower. Conversely, for a low value of $\alpha_{TH}$, the excess
509 pore water pressures close to the wall are very low, as was observed in Problem A. However, it should
510 be noted that, in the retaining wall problem, additional mechanical effects contribute to the generation
511 of pore water pressures, such as the thermal expansion of the wall. Furthermore, the presence of
512 additional free draining boundaries influences the rate of dissipation.

513 Similar to what was observed for Problem A, excess pore water pressures develop ahead of changes in
514 temperature, as marked on Figure 15. Indeed, at the beginning of the analysis (i.e. 10 days – $R$ = 0.05),
515 a high value of $\omega$ (51%) is obtained for a low value of $\alpha_{TH}$=1.6×10$^{-2}$, which rapidly decreases with
516 time due to the high rate of dissipation; conversely, considerably lower values are obtained for higher
517 values of $\alpha_{TH}$. It should be noted that, as mentioned earlier, in the retaining wall problem, due to the
518 presence of additional hydraulic boundary conditions, the dissipation process is accelerated.
519 Furthermore, the mechanical restriction in the horizontal direction along the right-hand side far field
520 boundary leads to mechanically induced pore water pressures similar to those observed in Problem B,
521 hence the increase with time observed for the high value of $\alpha_{TH}$.




522

523 *Figure 15: Distribution of change in temperature ΔT change in pore water pressure Δu along a horizontal line at mid-depth*
524 *of the wall for different time instants (a) ΔT, (b) Δu for $\alpha_{TH}$ = 2.6×10², (c) Δu for $\alpha_{TH}$ = 2.6×10⁰and (d) Δu for $\alpha_{TH}$ =*
525 *2.6×10 ⁻²*

### 4.3.2 *Influence on structural forces*

Figure 16 shows the effect of $\alpha_{TH}$ on the evolution with time of thermally-induced axial forces and bending moments. It confirms that the transient behaviour of a thermo-active retaining wall is largely controlled by the generated excess pore water pressures during the heating stage and by the ability of the soil to dissipate them. In fact, both phenomena lead to mechanical volumetric changes within the soil mass, which affect the mechanical response of the structure.

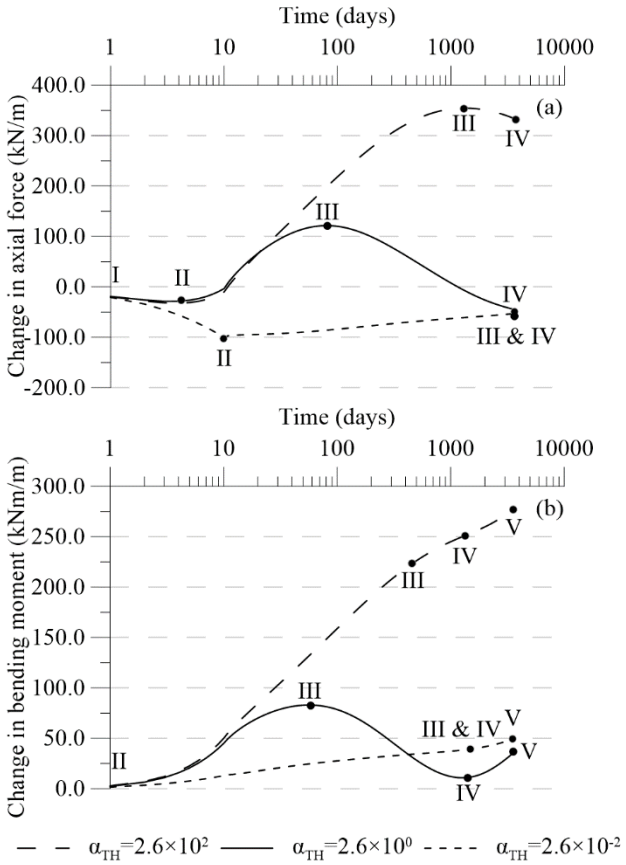



*Figure 16: Influence of $\alpha_{TH}$ on changes in (a) axial force at depth of 14.0 m bgl and (b) bending moment at depth of 10.5 m bgl*

In Figure 16 (a), the three previously identified phenomena affecting the development of axial force with time are highlighted, i.e. the restriction through shearing ("I-II"), thermal expansion ("II-III") and

dissipation of compressive pore water pressures ("III-IV"). The time periods over which each of these prevails depends directly on the value of $\alpha_{TH}$ – in some cases some of these phenomena may be even absent. The restriction through shearing along the soil-structure interface ("I-II") is larger for a lower value of $\alpha_{TH}$ because a small amount of compressive excess pore water pressures are generated. Consequently, the soil swells less, inducing a larger restriction to the structure, which leads to a larger initial compressive axial force. Conversely, although larger excess pore water pressures are generated for a higher value of $\alpha_{TH}$ (which would indicate more swelling), the axial force during the first 10 days of heating is rather similar to the base case which is characterised by an intermediate value of $\alpha_{TH}$. Interestingly, this suggests that the reduction of the restraint to the wall expansion resulting from soil swelling is compensated by its higher volumetric stiffness arising from behaving in a more undrained manner (i.e. its low permeability prevents additional changes in volume from taking place). In the long term, the axial force for the case of low $\alpha_{TH}$ is merely controlled by soil thermal expansion ("II-III"), hence a reduction in compressive axial force is observed. This is due to the fact that the low magnitudes of generated excess pore water pressures (see Figure 15 (d)), which also dissipate at a fast rate, do not contribute to changes in volume of the soil with time. On the other hand, with a high value of $\alpha_{TH}$, the period over which the axial force is governed by soil thermal expansion ("II-III") is larger in respect to the base case because excess pore water pressures dissipate at a slower pace and therefore the resulting changes in volume take place at a later stage of the analysis (i.e. "III-IV").

The evolutions with time of the bending moment (see Figure 16 (b)) confirm some of the patterns identified based on the variations of axial force. In effect, for the low value of $\alpha_{TH}$, the bending moment is seen to be mainly affected by soil thermal expansion ("II-III"), with the stage where the dissipation of compressive pore water pressures dominates wall response being completely absent ("III-IV"). The opposite is observed for the two other values of $\alpha_{TH}$, where this stage appears to have substantial impact (though it tends to be less important and to take place at a later stage for larger values of $\alpha_{TH}$). For all analysed cases, the final part of the evolutions with time of the binding moment of the wall seem to be fundamentally controlled by the effect of the mechanical restriction to thermal expansion imposed by the mechanical boundary condition at the axis of symmetry ("IV-V"), which had been previously

identified in the context of Problem B. Since the presence of this boundary condition affects only the horizontal response of the embedded part of the retaining wall, it is perhaps unsurprising to see it influencing only the bending moment and not the axial force.

## 5 Conclusions

In the design of thermo-active structures, various thermo-hydro-mechanical (THM) interactions within the soil need to be taken into account in order to understand and predict the mechanical response of the structure. This study focusses on the effect of these interactions on the behaviour of a thermo-active retaining wall by performing fully coupled THM finite element analyses. To identify clearly the origin and impact of different THM interactions, simulations of simple, one-dimensional problems were performed, where the effects of mechanical restrictions and soil properties were investigated.

Prior to performing the analyses of one-dimensional problems, analytical expressions for the calculation of excess pore water pressure and dimensionless parameters were defined in order to compare consistently simulations with different soil properties. The results of the analysed one-dimensional problems showed that:

- There are three main processes that lead to generation of excess pore water pressures in a fully coupled THM analysis, namely changes in temperature (thermally-induced), water flow (hydraulically-induced) and mechanical actions (mechanically-induced);
- These mechanisms depend on the thermal, hydraulic and mechanical boundary conditions as well as the soil properties. It was shown that the THM interactions are determined by the relative rate at which heat transfer and water flow progress. This was quantified through the dimensionless parameter $\alpha_{TH}$, expressed as the ratio of the thermal and hydraulic diffusivity;
- A direct correlation between $\alpha_{TH}$ and the pore water pressures generated at the heat source (i.e. thermally-induced), exists, where $\Delta u$ is highest for large values of $\alpha_{TH}$. Furthermore, the dissipation of the excess pore water pressures close to the heat source can also be related to this factor, where this happens earlier in time with lower $\alpha_{TH}$;

- Excess pore water pressures occur even before changes in temperatures occur. These are due to water flow (i.e. hydraulically-induced) and are time-dependent. While no direct correlation with $\alpha_{TH}$ can be established, it was shown that there are intermediate values of this parameter for which this phenomenon is enhanced.

The above-mentioned mechanisms of pore water pressure generation have been observed also in the simulations of the retaining wall problem. The parametric study on the effect of varying $\alpha_{TH}$ within the thermo-active retaining wall analysis has shown that the main conclusions drawn from the simulations on simple geometries are also applicable to more complex boundary value problems. However, it should be noted that, in such a context, the results will be affected by the presence of more complex drainage patterns than those enforced in the one-dimensional problems. These analyses have also shown that the THM interactions within the soil, and their transient nature, have a significant effect on the structural response of the wall, with different phenomena prevailing over different time periods, namely thermal soil expansion, volumetric deformations due to pore water generation and dissipation, and interactions with the mechanical boundary conditions (which depend on the geometry of the problem). Varying the ground properties, hence altering the thermo-hydro-mechanical response of the soil, led to important changes in the behaviour of the structure. According to these results, it is evident that adequate estimates of the hydraulic and thermal parameters of the soil are important to guarantee a safe and reliable design of thermo-active walls. Furthermore, in order to account for the various interactions that take place in such problems, fully coupled transient THM analyses are required.

## Acknowledgements

The PhD programme of the first author is sponsored by the Department of Civil and Environmental Engineering, Imperial College London, through a Skempton Scholarship.

## Appendix A Development of analytical expressions for excess pore water pressures in undrained conditions

According to Equation 2 in Section 2, the hydraulic equation in undrained conditions, with compression positive sign convention, is expressed as:

$$\frac{\Delta u}{K_f} n - 3n(\alpha_w - \alpha_s)\Delta T = \frac{\Delta p'}{K_s} \tag{A1}$$

615 Note that $p'$ is the mean effective stress (defined as $\left(\sigma'_x + \sigma'_y + \sigma'_z\right)/3$) and that $\Delta p'/K_s$ is equivalent
616 to the change in mechanical volumetric strain, $\Delta\varepsilon_{v,mech}$:

$$\Delta\varepsilon_{v,mech} = \Delta\varepsilon_{x,mech} + \Delta\varepsilon_{y,mech} + \Delta\varepsilon_{z,mech} \tag{A2}$$

617 where $\Delta\varepsilon_{x,mech}$, $\Delta\varepsilon_{y,mech}$, $\Delta\varepsilon_{z,mech}$ are the changes in the mechanical strains in the $x$, $y$, and $z$-
618 direction, respectively, which, according to Hooke's law for linear-elastic materials, are defined as:

$$\Delta\varepsilon_{x,mech} = \frac{\Delta\sigma'_x}{E} - \frac{\nu}{E}\left(\Delta\sigma'_y + \Delta\sigma'_z\right) \tag{A3}$$

619

$$\Delta\varepsilon_{y,mech} = \frac{\Delta\sigma'_y}{E} - \frac{\nu}{E}(\Delta\sigma'_x + \Delta\sigma'_z) \tag{A4}$$

620

$$\Delta\varepsilon_{z,mech} = \frac{\Delta\sigma'_z}{E} - \frac{\nu}{E}\left(\Delta\sigma'_x + \Delta\sigma'_y\right) \tag{A5}$$

621

622 Considering the problem depicted in Figure A. 1 (a), which is free to expand in the $x$-direction only,
623 the total strains ($\varepsilon_{tot} = \varepsilon_{mech} + \varepsilon_{th}$) along $y$ and $z$ are equal to zero and thus the mechanical strains in
624 these directions are equal to the thermal strain, $\varepsilon_{th} = -\alpha_s \cdot \Delta T$, but of opposite sign, i.e. $\alpha_s \cdot \Delta T$.
625 Furthermore, the total stress in the $x$-direction is equal to zero and hence the change in effective stress
626 is given by $\Delta\sigma'_x = -\Delta u$. As a consequence, equations A4 and A5 can be written as:

$$\frac{\Delta\sigma'_y}{E} - \frac{\nu}{E}(\Delta\sigma'_z - \Delta u) = \alpha_s \cdot \Delta T \tag{A6}$$

627

$$\frac{\Delta\sigma'_z}{E} - \frac{\nu}{E}\left(\Delta\sigma'_y - \Delta u\right) = \alpha_s \cdot \Delta T \tag{A7}$$

628

629 Which leads to:

$$\Delta\sigma'_y + \Delta\sigma'_z = \frac{2(E \cdot \alpha_s \cdot \Delta T - \nu \cdot \Delta u)}{(1-\nu)} \tag{A8}$$

630

631 Hence, the change in mean effective stress $\Delta p'$ is equal to:

$$\Delta p' = \frac{\left(\Delta\sigma'_x + \Delta\sigma'_y + \Delta\sigma'_z\right)}{3} = \frac{2}{3}\frac{(E \cdot \alpha_s \cdot \Delta T - \nu \cdot \Delta u)}{(1-\nu)} - \frac{\Delta u}{3} \tag{A9}$$

632

633 Noting that $3K_s = E/(1-2\nu)$, substituting equation A9 into Equation A1 allows the change in pore
634 water pressures to be expressed as:

$$\Delta u = \frac{3n(\alpha_w - \alpha_s) \cdot \Delta T}{\frac{n}{K_f} + \frac{1}{3K_s}\left(\frac{1+\nu}{1-\nu}\right)} + \frac{2\alpha_s\left(\frac{1-2\nu}{1-\nu}\right) \cdot \Delta T}{\frac{n}{K_f} + \frac{1}{3K_s}\left(\frac{1+\nu}{1-\nu}\right)} \tag{A10}$$

635 The problem depicted in Figure A. 1 (b) includes an additional restriction in the $x$-direction and thus
636 the mechanical strains in all directions are equal to $\alpha_s \cdot \Delta T$, which leads to:

$$\begin{aligned} \Delta\varepsilon_{v,mech} &= \Delta\varepsilon_{x,mech} + \Delta\varepsilon_{y,mech} + \Delta\varepsilon_{z,mech} \\ &= \Delta\sigma'_x + \Delta\sigma'_y + \Delta\sigma'_y - 2\nu\left(\Delta\sigma'_x + \Delta\sigma'_y + \Delta\sigma'_y\right) = 3E \cdot \alpha_s \cdot \Delta T \end{aligned} \tag{A11}$$

637 Which can be rewritten as

$$3\Delta p' = \frac{3E \cdot \alpha_s \cdot \Delta T}{(1-2\nu)} \tag{A12}$$

638

639 Thus:

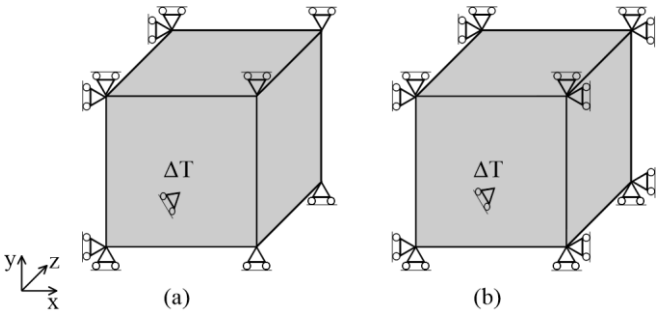
$$\Delta p' = \frac{E \cdot \alpha_s \cdot \Delta T}{(1-2\nu)} = 3K_s \cdot \alpha_s \cdot \Delta T \tag{A13}$$

640

641 Substituting Equation A13 into Equation A1 and rearranging, leads to the following expression for the
642 change in pore water pressures:

$$\Delta u = 3(\alpha_w - \alpha_s) \cdot K_f \cdot \Delta T + 3\alpha_s \cdot \frac{K_f}{n} \cdot \Delta T \tag{A14}$$

643




644 *Figure A. 1: Schematic representation of (a) one dimensional expansion and (b) fully restricted*

645 **Appendix B Analytical solutions for the calculation of temperature distribution through**
646 **solids of finite length**

647 The temperature distributions for different $x$-coordinates and time instants for Problem A can be
648 calculated analytically using the following expression (Carslaw and Jaeger, 1959):

$$\begin{aligned} &T(x,t) \\ &= T_0 + (T_1 - T_0)\frac{x}{L} \\ &+ \frac{2}{\pi}\sum_{n=1}^{\infty} \frac{T_1 \cos n\pi - T_0}{n} \sin\frac{n\pi x}{L} e^{-n^2\pi^2 Fo} + \sum_{1}^{\infty} \sin\frac{n\pi x}{L} e^{-n^2\pi^2 Fo} \int_0^L f(x') \cos\frac{(2n+1)\pi x'}{2L} dx' \end{aligned} \tag{B1}$$

649 where $T_0$ and $T_1$ are the temperatures imposed at coordinates $x = 0$ and $x = L$, respectively, and
650 $\int_0^L f(x')dx'$ is the function of the initial temperature distribution. For the special case of a constant
651 initial temperature distribution of 0°C or if changes in temperature from an initially constant

temperature distribution wish to be calculated, then one of the fixed temperatures will have a value of 0°C and Equation B1 reduces to:

$$T(x,t) = T_0 + (T_1 - T_0)\frac{x}{L} + \frac{2}{\pi}\sum_{n=1}^{\infty}\frac{T_1 \cos n\pi - T_0}{n}\sin\frac{n\pi x}{L}e^{-n^2\pi^2 Fo} \quad \text{(B2)}$$

Similarly, the equation below (Carslaw and Jaeger, 1959) allows the calculation of the temperature distributions for the case where the boundary at $x = 0$ is insulated and $x = L$ is kept at constant temperature $T_0$ and with an initial temperature profile $f(x)$, hence simulating the conditions of Problem B:

$$T(x,t) = T_0 + \frac{2}{L}\sum_{n=0}^{\infty} e^{-(2n+1)^2\pi^2 Fo/4}\cos\frac{(2n+1)\pi x}{2L}\left\{\frac{2L(-1)^{n+1}T_0}{(2n+1)\pi} + \int_0^L f(x')\cos\frac{(2n+1)\pi x'}{2L}dx'\right\} \quad \text{(B3)}$$

For the conditions mentioned above, the problem can be simplified to:

$$T(x,t) = T_0 + \frac{2}{L}\sum_{n=0}^{\infty} e^{-(2n+1)^2\pi^2 Fo/4}\cos\frac{(2n+1)\pi x}{2L}\left\{\frac{2L(-1)^{n+1}T_0}{(2n+1)\pi}\right\} \quad \text{(B4)}$$

## Appendix C Soil models and properties for retaining wall problem

Concrete was modelled as a linear-elastic material with a stiffness of 30 GPa, as indicated in Wood and Perrin (1984). The Made Ground was modelled as a linear elasto-plastic material with a Mohr-Coulomb failure surface. All other soil layers were modelled as non-linear elasto-plastic materials with a Mohr-Coulomb failure surface and the IC.G3S non-linear elastic stiffness model (Taborda et al., 2016). For consolidating materials, i.e. London Clay and Lambeth Group Clay, a non-linear permeability model was adopted, where the permeability decreases with increasing mean effective stress, $p'$, according to the following relationship:

$$k = k_0 e^{-Bp'} \tag{C1}$$

where the parameters $k_0$ and $B$ are model parameters. $k_0$= $10^{-10}$ an $B$=0.023.

With the exception of Made Ground, the pre-yield behaviour of all the other soils is assumed to be reproduced by the non-linear small-strain stiffness model proposed by Taborda et al. (2016). According to this model, the tangent shear modulus, $G_{tan}$, is given by:

$$G_{tan} = G_{max} \cdot \left[ R_{G,min} + \frac{1 - R_{G,min}}{1 + \left(\frac{E_d}{a}\right)^b} \right] \geq G_{min} \tag{C2}$$

where $E_d$ is the second invariant of the strain tensor (see Equation C3), $G_{min}$ is the minimum shear stiffness and $a$, $b$ and $R_{G,min}$ are model parameters.

$$E_d = \left( \frac{4}{6} \cdot \left[ \left(\varepsilon_x - \varepsilon_y\right)^2 + \left(\varepsilon_y - \varepsilon_z\right)^2 + \left(\varepsilon_z - \varepsilon_x\right)^2 \right] + {\gamma_{xy}}^2 + {\gamma_{yz}}^2 + {\gamma_{xz}}^2 \right)^{\frac{1}{2}} \tag{C3}$$

In Equation C2, the maximum shear stiffness, $G_{max}$, is calculated using:

$$G_{max} = G_0 \cdot \left( \frac{p'}{{p'}_{ref}} \right)^{m_G} \tag{C4}$$

where $p'$ is the mean effective stress, $p'_{ref}$ is a reference pressure (assumed to be equal to the atmospheric pressure, i.e. 101.3 kPa), while $G_0$ and $m_G$ are model parameters (in this paper, the latter is assumed to be 1.0, i.e. the shear stiffness varies linearly with $p'$).

Similarly, the tangent bulk modulus, $K_{tan}$, is given by:

$$K_{tan} = K_{max} \cdot \left[ R_{K,min} + \frac{1 - R_{K,min}}{1 + \left(\frac{|\varepsilon_v|}{r}\right)^s} \right] \geq K_{min} \tag{C5}$$

where $\varepsilon_v$ is the volumetric strain (i.e. the first invariant of the strain tensor, see Equation C6), $K_{min}$ is the minimum bulk modulus and $r$, $s$ and $R_{K,min}$ are model parameters.

$$\varepsilon_v = \varepsilon_x + \varepsilon_y + \varepsilon_z \tag{C6}$$

In Equation C5, the maximum bulk modulus, $K_{max}$, is calculated using:

$$K_{max} = K_0 \cdot \left( \frac{p'}{p'_{ref}} \right)^{m_K} \quad \text{(C7)}$$

where $K_0$ and $m_K$ are model parameters (as for the shear stiffness, the latter is assumed to be 1.0, i.e. the bulk modulus varies linearly with $p'$).

The tables below summarise the linear and non-linear mechanical properties, as well as the thermal properties, of the concrete structure and soil layers employed in all analyses.

| Material | $E$ [kPa] | $\nu$ [--] |
|---|---|---|
| Concrete | $30\times10^6$ | 0.3 |
| Made Ground | $10\times10^3$ | 0.2 |

*Table C. 1: Linear elastic properties*

| Material | $c'$ [kPa] | $\varphi'$ [°] | $\psi'$ [°] |
|---|---|---|---|
| Made Ground | 0.0 | 30.0 | 0.0 |
| Terrace Gravel | 0.0 | 35.0 | 17.5 |
| London Clay | 5.0 | 25.0 | 12.5 |
| Lambeth Group Clay | 25.0 | 27.0 | 13.5 |
| Thanet Sand | 0.0 | 40.0 | 20.0 |

*Table C. 2: Mohr-Coulomb strength properties*

| Material | $G_0$ [kPa] | $a$ [--] | $b$ [--] | $R_{G,min}$ [kPa] | $G_{min}$ [kPa] |
|---|---|---|---|---|---|
| Terrace Gravel | 41939.61 | 0.000145 | 1.0 | 0.03511 | 3000 |
| London Clay | 51743.55 | 0.000056 | 0.9 | 0.06450 | 2667 |
| Lambeth Group Clay | 51924.52 | 0.000110 | 0.95 | 0.04662 | 2667 |
| Thanet Sand | 65275.23 | 0.000046 | 0.85 | 0.02631 | 2000 |

*Table C. 3: Small strain stiffness properties*

| Material | $K_0$ [kPa] | $r$ [--] | $s$ [--] | $R_{K,min}$ [kPa] | $K_{min}$ [kPa] |
|---|---|---|---|---|---|
| Terrace Gravel | 49843.08 | 0.000247 | 1.25 | 0.15440 | 3000 |
| London Clay | 26692.73 | 0.000127 | 1.8 | 0.13275 | 5000 |
| Lambeth Group Clay | 61331.71 | 0.000065 | 1.4 | 0.07589 | 5000 |
| Thanet Sand | 29813.53 | 0.000155 | 1.1 | 0.27947 | 5000 |

*Table C. 4: Small strain stiffness properties*

| Material | $\gamma_s$ [kN/m$^3$] | $\alpha_s$ [m/mK] | $\alpha_w$ [m/mK] | $K_f$ [GPa] | $\rho C_p$ [kJ/m$^3$K] | $\lambda$ [W/mK] |
|---|---|---|---|---|---|---|
| Concrete | 24.0 | $8.5\times10^{-6}$ | -- | -- | -- | -- |
| Made Ground | 18.0 | $1.7\times10^{-5}$ | --(*) | --(*) | 1900 | 1.40 |
| Terrace Gravel | 20.0 | $1.7\times10^{-5}$ | --(*) | --(*) | 1900 | 1.40 |
| London Clay | 20.0 | $1.7\times10^{-5}$ | $6.9\times10^{-5}$ | 2.2 | 1820 | 1.79 |
| Lambeth Group Clay | 20.0 | $1.7\times10^{-5}$ | $6.9\times10^{-5}$ | 2.2 | 1760 | 2.20 |
| Thanet Sand | 20.0 | $1.7\times10^{-5}$ | --(*) | --(*) | 1760 | 2.40 |

(*) parameter not required since stratum is considered fully drained

*Table C. 5: Thermal and thermo-mechanical material properties (adopted from Gawecka et al., 2017)*

## References


Abuel-Naga, H. M., Bergado, D. T., Bouazza, A., 2007a. Thermally induced volume change and excess pore water pressure of soft Bangkok clay. *Engineering Geology*. **89(1-2)**, 144-154.

Abuel-Naga, H. M., Bergado, D. T., Bouazza, A., Ramana, G. V., 2007b. Volume change behaviour of saturated clays under drained heating conditions: Experimental results and constitutive modeling. *Canadian Geotechnical Journal*. **44(8)**, 942-956.

Baldi, G., Hueckel, T., Pellegrini, R., 1988. Thermal volume changes of the mineral-water system in low-porosity clay soils. *Canadian Geotechnical Journal*. **25(4)**, 807-825.

Barla, M., Di Donna, A., Santi, A., 2020. Energy and mechanical aspects on the thermal activation of diaphragm walls for heating and cooling. *Renewable Energy*. **147**, 2654-2663.

Bourne-Webb, P., Freitas, T. B., Assunção, R. F., 2019. A review of pile-soil interactions in isolated, thermally-activated piles. *Computers and Geotechnics*. **108**, 61-74.

Bourne-Webb, P. J., Amatya, B., Soga, K., Amis, T., Davidson, C., Payne, P., 2009. Energy pile test at Lambeth College, London: geotechnical and thermodynamic aspects of pile response to heat cycles. *Géotechnique*. **59(3)**, 237-48.

Brandl, H., 2006. Energy foundations and other thermo-active ground structures. *Géotechnique*. **56 (2)**, 81-122.

Carslaw, H. S., Jaeger, J. C., 1959. *Conduction of heat in solids.* 2nd ed. Clarendon Press, Oxford.

Cekerevac, C., Laloui, L., 2004. Experimental study of thermal effects on the mechanical behaviour of a clay. *International Journal for Numerical and Analytical Methods in Geomechanics*. **28(3)**, 209-228.

Craig, R. F., 2004. *Craig's soil mechanics.* 7th ed. Spon Press/Taylor Francis, London.

Cui, W., Gawecka, K. A., Taborda, D. M. G., Potts, D. M., Zdravković, L., 2016. Time-step constraints in transient coupled finite element analysis. *International Journal for Numerical Methods in Engineering*. **106(12)**, 953-971.

Cui, W., Potts, D. M., Zdravković, L., Gawecka, K. A. , Taborda, D. M. G., 2018. An alternative coupled thermo-hydro-mechanical finite element formulation for fully saturated soils. *Computers and Geotechnics*. **94**, 22-30.

Dai, Q., Li, Z., 2019. Long-term mechanical performance of geothermal diaphragm walls in stiff clay. *Tunnelling and Underground Space Technology*. **94**, 103-113.

Di Donna, A., Laloui, L., 2015. Numerical analysis of the geotechnical behaviour of energy piles. *International Journal for Numerical and Analytical Methods in Geomechanics*. **39(8)**, 861-888.

Di Donna, A., Rotta Loria, A. F., Laloui, L., 2016. Numerical study of the response of a group of energy piles under different combinations of thermo-mechanical loads. *Computers and Geotechnics*. **72**, 126-142.

Dupray, F., Laloui, L., Kazangba, A., 2014. Numerical analysis of seasonal heat storage in an energy pile foundation. *Computers and Geotechnics*. **55**, 67-77.

Gatmiri, B., Delage, P., 1997. A formulation of fully coupled thermal–hydraulic–mechanical behaviour of saturated porous media - numerical approach. *International Journal for Numerical and Analytical Methods in Geomechanics*. **21(3)**, 199-225.

Gawecka, K. A., Taborda, D. M. G., Potts, D. M., Cui, W., Zdravković, L., Haji Kasri, M. S., 2017. Numerical modelling of thermo-active piles in London Clay. *Proceedings of the Institution of Civil Engineers: Geotechnical Engineering*. **170(3)**, 201-219.

Jeong, S., Lim, H., Lee, J. K., Kim, J., 2014. Thermally induced mechanical response of energy piles in axially loaded pile groups. *Applied Thermal Engineering*. **71(1)**, 608-615.

Jorgensen, D. G., 1980. *Relationships between basic soils-engineering equations and basic ground-water flow equations*. Office, U. S. G. P., Washington, Report 2064.

Laloui, L., Francois, B., 2009. ACMEG-T: Soil thermoplasticity model. *Journal of Engineering Mechanics*. **135(9)**, 932-944.

Laloui, L., Nuth, M., Vulliet, L., 2006. Experimental and numerical investigations of the behaviour of a heat exchanger pile. *International Journal for Numerical and Analytical Methods in Geomechanics*. **30(8)**, 763-781.

Lewis, R. W., Schrefler, B. A., 1998. *The finite element method in the static and dynamic deformation and consolidation of porous media.* John Wiley.

Liu, R. Y. W., Sailer, E., Taborda, D. M., Potts, D. M., Zdravković, L., 2020. A practical method for calculating thermally-induced stresses in pile foundations used as heat exchangers. *Computers and Geotechnics*. **126**, 103743.

Loveridge, F., Powrie, W., 2013. Pile heat exchangers: Thermal behaviour and interactions. *Proceedings of the Institution of Civil Engineers - Geotechnical Engineering*. **166(2)**, 178-196.

Makasis, N., Narsilio, G. A., Bidarmaghz, A., 2018. A machine learning approach to energy pile design. *Computers and Geotechnics*. **97**, 189-203.

Ng, C. W. W., Shi, C., Gunawan, A., Laloui, L., 2014. Centrifuge modelling of energy piles subjected to heating and cooling cycles in clay. *Géotechnique Letters*. **4(4)**, 310-316.

Olivella, S., Gens, A., Carrera, J., Alonso, E. E., 1996. Numerical formulation for a simulator (CODE_BRIGHT) for the coupled analysis of saline media. *Engineering Computations*. **13(7)**, 87-112.

Potts, D. M., Zdravković, L., 1999. *Finite Element Analysis in Geotechnical Engineering: Theory.* Thomas Telford, London.

Rui, Y., Yin, M., 2018. Thermo-hydro-mechanical coupling analysis of a thermo-active diaphragm wall. *Canadian Geotechnical Journal*. **55(5)**, 720-735.

Sailer, E., Taborda, D. M., Zdravković, L., Potts, D. M., 2019a. Fundamentals of the coupled thermo-hydro-mechanical behaviour of thermo-active retaining walls. *Computers and Geotechnics*. **109**, 189-203.

Sailer, E., Taborda, D. M. G., Zdravkovic, L., Potts, D. M., 2019b. Numerical modelling of thermo-active shafts, in Ferrari, A., andLaloui, L. (Eds), *Energy Geotechnics*. Springer, Berlin, pp. 97-104.

Salciarini, D., Ronchi, F., Tamagnini, C., 2017. Thermo-hydro-mechanical response of a large piled raft equipped with energy piles: a parametric study. *Acta Geotechnica*. **12(4)**, 703-728.

Sterpi, D., Tomaselli, G., Angelotti, A., 2020. Energy performance of ground heat exchangers embedded in diaphragm walls: Field observations and optimization by numerical modelling. *Renewable Energy*. **147**, 2748-2760.

Stewart, M. A., Mccartney, J. S., 2013. Centrifuge modeling of soil-structure interaction in energy foundations. *Journal of Geotechnical and Geoenvironmental Engineering*. **140(4)**, 04013044.

Sultan, N., Delage, P., Cui, Y. J., 2002. Temperature effects on the volume change behaviour of Boom clay. *Engineering Geology*. **64(2-3)**, 135-145.

Taborda, D. M. G., Potts, D. M., Zdravković, L., 2016. On the assessment of energy dissipated through hysteresis in finite element analysis. *Computers and Geotechnics*. **71**, 180-194.

Thomas, H. R., He, Y., 1997. A coupled heat–moisture transfer theory for deformable unsaturated soil and its algorithmic implementation. *International Journal for Numerical Methods in Engineering*. **40(18)**, 3421-3441.

Wood, L. A., Perrin, A. J., 1984. Observations of a strutted diaphragm wall in London clay: A preliminary assessment. *Géotechnique*. **34(4)**, 563-579.